

Research Paper

Performance of high-concentration photovoltaic cells cooled by a hybrid microchannel heat sink

Yousef Alihosseini^{a,b,c,1}, Yaser Oghabneshin^{c,1}, Amir Rezazad Bari^c, Sahel Moslemi^d, Ahmad Reza Roozbehi^c, Mohammad Zabetian Targhi^{c,*}, Wei Guo^{a,b,*}

^a Mechanical Engineering Department, FAMU-FSU College of Engineering, Florida State University, Tallahassee, FL 32310, USA

^b National High Magnetic Field Laboratory, 1800 East Paul Dirac Drive, Tallahassee, FL 32310, USA

^c Mechanical Engineering Department, Tarbiat Modares University, Tehran, Iran

^d Chemical Engineering Department, Sahand University of Technology, Tabriz, Iran

ARTICLE INFO

Keywords:

High-concentration photovoltaic cell
Efficient cooling
Hybrid configuration
Oblique microchannel
Micro Pin fin
Pumping power

ABSTRACT

The electrical performance and equipment lifetime of high-concentration photovoltaic cells depends heavily on efficient cooling. In this paper, we applied a hybrid configuration to the cooling of a high-concentration photovoltaic cell, an innovative pattern derived from a comprehensive study on the combination of oblique microchannel and micro pin fin. Results from this study found that an elliptical pin fin pattern conforming with streamlines most effectively removed heat flux with a Nusselt number of 65.44 at a Reynolds number 1250. Then, the performance evaluation of a photovoltaic cell with a concentration ratio of 1000 was carried out on the hottest day of each season in Shiraz under actual boundary conditions. With an average flow rate of 30 ml/min in the spring, the implementation of this hybrid design resulted in the photovoltaic cell achieving an electrical efficiency of 40.16 while still maintaining a constant surface temperature of 301 K. Unlike a straight microchannel, which failed to maintain a constant cell temperature throughout summer's hottest hours, this hybrid configuration succeeded in sustaining cooling with an average flow rate of 90 ml/min. In the winter and autumn, the pump's average power consumption required for cooling was about 25 and 38 mW, respectively. Moreover, the maximum output electrical power in the summer was 2.8 W, with pumping power contributing to 1500 mW.

1. Introduction

To satisfy the growing demand for affordable, renewable energy, the use of photovoltaic (PV) systems to generate power through solar radiation has increased [1,2]. The performance, efficiency, and lifespan of PV cells depend heavily on climatic factors such as wind speed, wind direction, and ambient temperature [3,4]. Research shows that a temperature increase of 1 °C leads to a 0.5 % performance decline in PV cells [5]. To combat this, researchers have attempted to develop efficient cooling techniques for heat dissipation from PV modules [6,7] including air cooling [8,9], heat pipes [10,11], and microchannel heat sinks (MCHSs) [12,13]. MCHSs have recently been of greater interest to thermal engineers due to their large area-to-volume ratio, ease of use, and efficiency in removing high heat flux. Numerous studies have been conducted on the thermal performance enhancement of MCHSs in recent years. Flow parameters, such as nanofluid, boiling, and pulsating flow

[14,15], as well as geometric factors, like channel pattern and cross-section, play critical roles in enhancing an MCHS's performance [16]. Existing literature on PV cell cooling using MCHSs primarily focuses on changing the channel pattern to improve thermal efficiency [17,18]. Furthermore, recent studies have explored various geometric microchannel patterns, such as sinusoidal, oblique grooved, and pin fin [19–22]. Oblique grooved and pin fin MCHSs are particularly significant due to their larger wetted areas and higher rates of flow mixing [23,24]. In a parametric investigation of heat transfer enhancement in grooved MCHSs, Lee et al. [25] report that a higher flow rate improved flow diffusion into transverse grooves, thereby increasing flow mixing. Increased flow mixing coupled with the disruption of thermal boundary layers led to a marked improvement of heat transfer in the grooved pattern compared to the straight one. Alihosseini et al. [26] designed a new MCHS pattern featuring a combination of oblique grooved fins and wavy MCHS. Results illustrate that this hybrid design was more efficient

* Corresponding authors.

E-mail addresses: zabetian@modares.ac.ir (M.Z. Targhi), wguo@magnet.fsu.edu (W. Guo).

¹ These authors contributed equally: Yousef Alihosseini and Yaser Oghabneshin.

than a simple wavy one due to its generation of secondary flow that increased the rate of heat transfer.

Yang et al. [27] examines various pin fin shapes, including circular, square, hexagonal, pentagonal, and triangular. They found that triangular pin fins caused maximum flow blockage, while circular ones caused the least. Flow blockage directly affects a system's pressure drop. Similarly, in a numerical study, Zhao et al. [28] assess the effects of circular, triangular, diamond, and pentagonal cross-sections on thermal performance. The strong vortices around the pin fin meant that the pentagonal cross-sections exhibited the best performance in terms of heat transfer coefficient and temperature uniformity.

Chen et al. [12] investigate using a serpentine microchannel to cool concentrated PV cells. They report that the serpentine microchannel improved cell temperature distribution uniformity and reduced the maximum cell temperature. Furthermore, their findings indicate that the electrical efficiency of the PV module experienced a 115 % increase due to maximum cell temperature reduction. Eesam et al. [29] explore the synergistic cooling effects of using both an input jet and an MCHS for concentrated PV panels. They employed a rectangular pin fin configuration in the flow direction. Their study suggests that the combination of an input jet and an MCHS enhanced cell temperature uniformity and reduced the maximum cell temperature at the maximum solar irradiance. Additionally, Abdallah Y. M. et al. [30] study the impact of flow direction on thermal performance by altering inlet and outlet configurations. An 11.4 % decrease in average cell temperature illustrated that the new convergent-divergent MCHS design achieved a better heat transfer rate compared to the conventional straight MCHS design for high concentrator photovoltaic module thermal management. To cool PV modules, Radwan et al. [31] evaluate various heat sink designs such as (a) a rectangular microchannel, (b) a single-layer parallel flow, (c) a single-layer counter-flow, (d) a double-layer parallel flow, and (e) a double-layer counter flow heat sink. Among these designs, the single-layer parallel-flow heat sink had the highest net cell power and electrical efficiency, as well as the lowest cell temperature at a CR = 20. In another study, Yang et al. [30] employ a multi-manifold microchannel cooling system with a rectangular design to mitigate and enhance the uniformity of PV cell temperature. Remarkably, they managed to maintain an average temperature of approximately 37 °C at CR = 70. On the other hand, the single-layer counter-flow MCHS exhibited the lowest performance.

Based on reviewed literature, it is evident that oblique microchannel heat sinks and pin fin configurations play a significant role in enhancing thermal performance. However, most of these aforementioned studies concentrate solely on individual patterns. The motivation to employ a hybrid design of oblique grooved microchannels with pin fins stems from the intrinsic trade-offs between heat transfer and pressure drop in heat sink configurations. Despite significantly improving heat transfer by introducing secondary flows and disruptions, oblique grooved microchannels inherently introduce a higher pressure drop compared to basic pin fin designs. To mitigate this, our design integrates pin fins within the MCHS. By strategically placing pin fins in the middle of the heat sink, the flow is less aggressively disrupted than as seen with oblique grooves, thereby reducing the overall pressure drop.

The hybrid pattern design, our research's central innovation, attempts to address two main concerns from previous configurations: hotspots caused by inconsistent temperature distribution, and decreases of Nusselt numbers along the channel. In this paper, we used numerical simulations to explore the effect of a hybrid pattern on the cooling of high-concentration photovoltaic cells. Initially, a comprehensive analysis of the combination of an oblique MCHS and 19 pin fin cross-sections was carried out to determine the pattern with the highest thermal performance. Subsequently, the optimal design was employed to effectively cool a high-concentration photovoltaic cell under actual boundary conditions (simultaneous surface radiation and free convection) in the city of Shiraz on the hottest day of each season. By comparing the hybrid and straight MCHS models, we were able to explore the impact of

efficient cooling on the photovoltaic cell's operational parameters, such as coolant flow velocity on cell temperature uniformity, net solar cell power, and pump power consumption.

2. Model design

Fig. 1 depicts a schematic view of an HCPV working principle. The proposed system is comprised of a concentration lens, an HPVC cell, and an MCHS. The solar concentration lens is utilized to focus solar radiation on the target in the solar cell. Capable of incorporating a biaxial tracking system, these concentrators can achieve a concentration ratio of 100 while still maintaining cost-effectiveness per power unit. The study utilizes a high-performance triple-junction HCPV cell, the latest version of the AZURE SPACE product [32]. As illustrated in Fig. 2, this solar cell is comprised of four layers. To generate electricity, the top layer features GaInP and GaInAs on a Germanium substrate. The bottom layers, on the other hand, consist of two Cu layers as well as one made from ceramic. Table 1 details the thermal properties and dimensions of these solar cell layers.

As depicted in Fig. 2, the MCHS, covering the rear side of the solar cell and board assembly, combines oblique microchannels with circular micro pin fins, effectively dissipating the generated heat. Fig. 3 features a detailed depiction of the hybrid MCHS's configurations. This hybrid model possesses three grooved rows, each with a width of 375 μm, as well as three straight rows with varied pin fin shapes. Additionally, the pin fin pattern, occupying one-third of the MCHS length, is situated between the pair of oblique grooved designs. In the first step, a comprehensive study was conducted to determine the most efficient hybrid pattern by analyzing the diverse cross-section shapes of 19 pin fin patterns. The chosen geometries are relevant for industrial applications. Table 2 provides detailed dimensions related to the various pin fins. All pin fins were sized such that they would have the same hydraulic diameter, thereby enabling efficient pattern comparison. Since the microchannel with a 25 mm × 25 mm dimension is symmetric, it was partially simulated to save computation time and cost. Therefore, three channels, as shown in Fig. 4, were simulated and discussed.

3. Numerical methodology

ANSYS Fluent V. R2 2021, based on the finite volume method (FVM), was employed to simultaneously simulate the system and solve the flow and heat transfer equations in the solid and liquid phases. The second-order upwind scheme was used to discretize the momentum and energy equations, while a standard discretization technique was used to discretize the pressure equation. The SIMPLE algorithm was adopted to couple velocity and pressure.

3.1. Governing equations

This study incorporated two distinct parts. Initially, various configurations were examined, excluding the high-concentration photovoltaic cells, to derive the optimal design with the highest thermal performance. Subsequently, this design effectively cooled a high-concentration photovoltaic cell exposed to varying solar irradiation levels. Some assumptions were considered for solving these equations, including [3,32,35,36]:

- 1) The solid materials have isotropic and temperature-dependent thermophysical properties, and water is used as a coolant to remove heat due to its high specific heat capacity.
- 2) Thermal contact resistance is negligible between the HCPV layers and MCHS.
- 3) The MCHS contains a steady-state, laminar, and incompressible flow (the local Reynolds number is below the critical Reynolds number of 2200 at the peak flow rate).
- 4) Viscous dissipation is neglected.

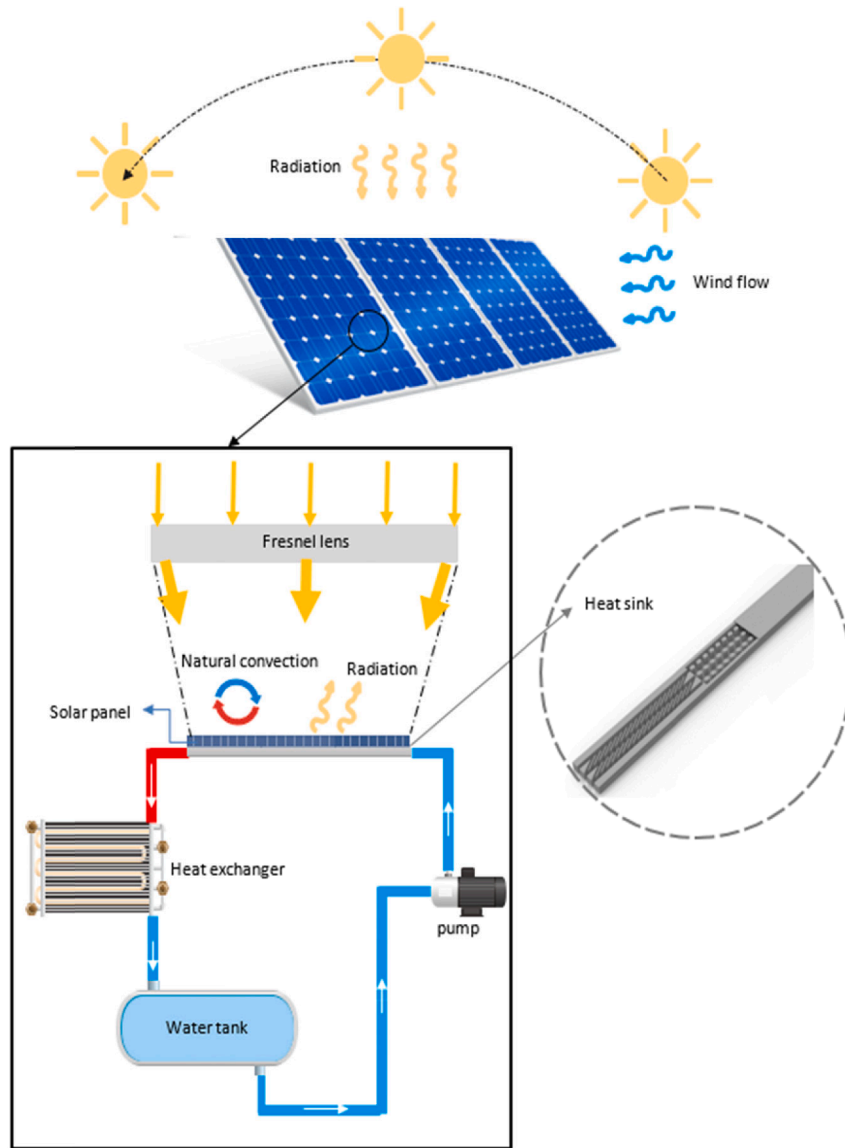


Fig. 1. A schematic view of an HCPV working principle.

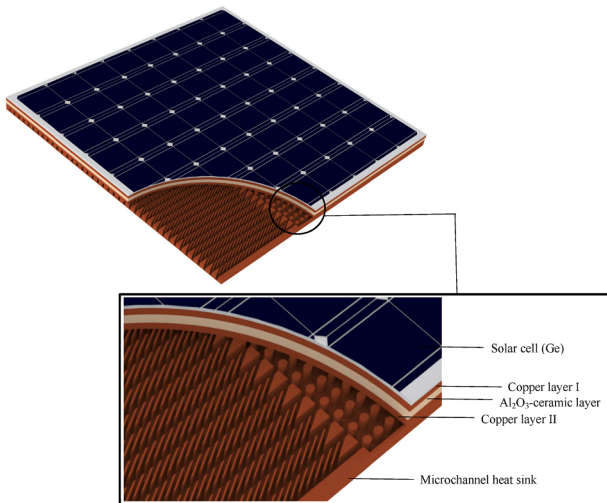


Fig. 2. A 3D schematic view of the HCPV cell.

Table 1

The specifications of junctions applied to the HCPV cell [33,34].

Solar cell layers	Thickness (mm)	K (W/m·K)	C (J/kg·K)	ρ (kg/m ³)	Emissivity (ϵ)
Germanium	0.19	60	320	5323	0.9
Copper-I	0.25	401	384	8933	0.05
Al ₂ O ₃ -ceramic	0.32	30	900	3900	0.75
Copper-II	0.25	401	384	8933	0.05

Accordingly, the governing equations are written as:

HCPV cell equations:

The heat produced in the different layers of the solar cell was obtained from the following equation [29,37]:

$$q_{Ge} = \frac{(1 - \eta_{cell}) G \alpha_{Ge} A}{V} \quad (1)$$

In the above equation, η_{cell} is the electrical efficiency of the solar cell; G is the net solar irradiance on the front surface of the Germanium layer, which is a function of the solar concentration ratio; α_{Ge} is Germanium's

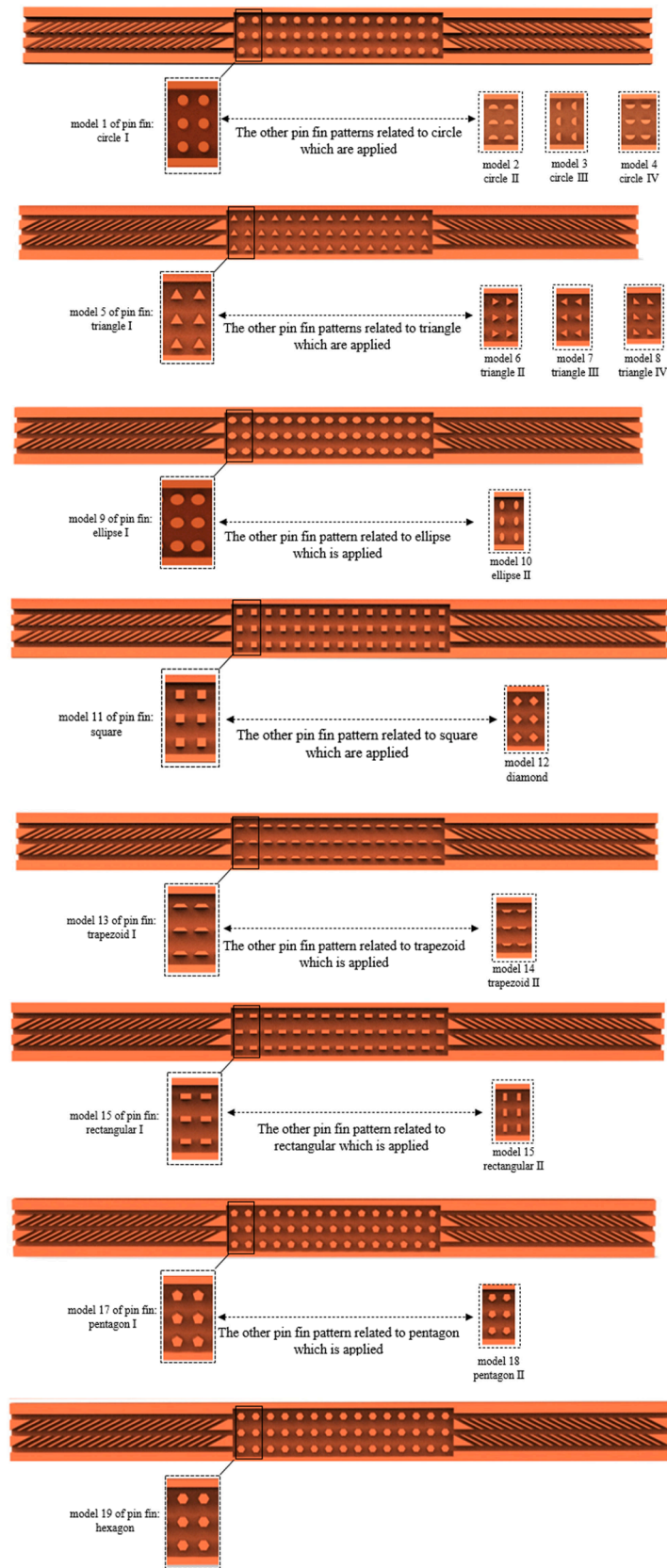


Fig. 3. The diverse geometries of pin fins used for the hybrid configuration.

Table 2
The geometric parameters of the pin fins.

Name	Circle I	Circle II	Circle III	Circle IV	Triangle I	Triangle II
Shape						
Area (μm ²)	60,000	50,000	50,000	50,000	40,000	40,000
Name	Triangle III	Triangle IV	Ellipse I	Ellipse II	Square	Diamond
Shape						
Area (μm ²)	40,000	30,000	80,000	80,000	50,000	50,000
Name	Trapezoid I	Trapezoid II	Rectangle I	Rectangle II	Pentagon I	Pentagon II
Shape						
Area (μm ²)	30,000	40,000	40,000	60,000	50,000	50,000
Name	Hexogen					
Shape						
Area (μm ²)	50,000					

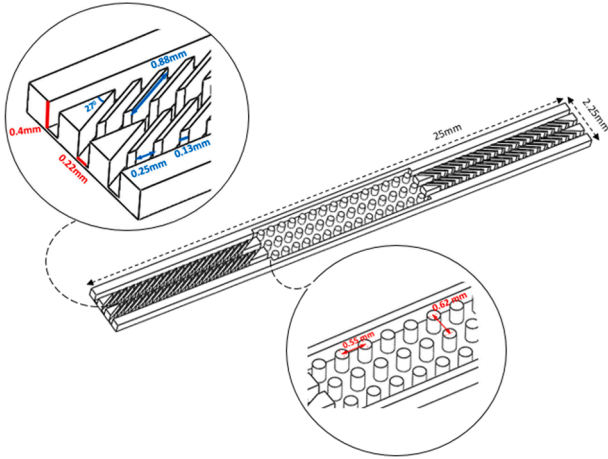


Fig. 4. The dimension of simulated geometry.

absorptivity; and A and V are the top surface area and volume of the Germanium layer, respectively.

The electrical performance of the solar cell is [38]:

$$\eta_{cell} = \eta_{Ref} - [\beta_{thermal}(T_{cell} - T_{Ref})] \quad (2)$$

$\eta_{Ref} = 40.3\%$, which is the electrical efficiency of the solar cell at

$T_{Ref} = 25^\circ\text{C}$ and $CR = 1000$ [39]. $\beta_{Thermal}$ is the thermal coefficient of Germanium and is equal to 0.047% [32]. Additionally, the solar cell electrical power, heat sink friction power, and net gained electrical power of the solar cell were calculated using the following equations [17,29]:

$$P_{el} = \eta_{cell} G \alpha_{cell} A \quad (3)$$

$$P_{friction} = \left(\frac{\dot{m}}{\rho_f}\right) \cdot \Delta P \quad (4)$$

$$P_{net} = P_{el} - P_{friction} \quad (5)$$

ΔP is the pressure drop across the microchannel heat sink, and m is the fluid mass flow rate.

MCHS equations [20,40]:

Conservation of mass:

$$\rho_f \nabla \cdot (\vec{U}) = 0 \quad (6)$$

Momentum equation:

$$\rho_f (\vec{U} \cdot \nabla) \vec{U} = -\nabla p + \mu \nabla^2 \vec{U} \quad (7)$$

The energy equation of the liquid:

$$\rho_f C_{pf} (\vec{U} \cdot \nabla T) = \nabla \cdot [k_f \nabla T] \quad (8)$$

The energy equation of the solid body:

$$\nabla \cdot [k_s \nabla T] = 0 \quad (10)$$

In the given equations, U , P , ρ_f , μ , C_{pf} , and k_f are the velocity vector, pressure, fluid density, dynamic viscosity, specific heat, and thermal conductivity, respectively. Furthermore, k_s is the solid thermal conductivity.

Local fluid temperature:

$$T_{f,x} = \frac{\int_{A_c} \rho_f u C_{pf} T dA_c}{\int_{A_c} \rho_f u C_{pf} dA_c} \quad (11)$$

The average local temperature of the microchannel wall is presented by the following equation:

$$T_{w,x} = \frac{1}{w} \int_w T_w dw \quad (12)$$

Then, the local heat transfer coefficient was calculated by the following equation:

$$h_x = \frac{q'' A_b}{(T_{w,x} - T_{f,x}) A_i} \quad (13)$$

In this equation, q'' is the heat flux, A_b is the base area of the channel that the heat flux applied to it, and A_i is the fluid–solid interface area that the coolant removes the heat from it. Additionally, $T_{w,x}$ and $T_{f,x}$ represent the local wall temperature and the local fluid bulk temperature.

Equations (14) and (15) calculated the local and average Nusselt number of the microchannel:

$$Nu_x = \frac{h_x D_h}{k_f} \quad (14)$$

$$Nu = \frac{1}{L} \int_L Nu_x dx \quad (15)$$

Where L is the length of the channel, k_f is the fluid thermal conductivity, and D_h is the channel hydraulic diameter as defined by:

$$D_h = \frac{4A_{ch}}{P} \quad (16)$$

A_{ch} and P are the cross-section and perimeter of the channel inlet plenum, respectively [41].

The pressure drop and friction factor were calculated by the following equations:

$$\Delta P = P_{in} - P_{out} \quad (17)$$

$$f = \frac{2 \Delta P D_h}{\rho_f L U^2} \quad (18)$$

3.2. Boundary conditions

As previously highlighted, this study incorporated two distinct sections with unique boundary conditions. Fig. 5 depicts the boundary condition for the first section focusing on deriving the optimal thermal performance of the microchannel. As shown, the inlet velocity of the microchannel was assumed to be uniform. The output pressure was set to atmospheric pressure, while the bottom surface was presumed to be adiabatic. Furthermore, the boundary condition at the side walls was considered as symmetry. Simulations operated at $Re = 1250$ with a constant heat flux of 80 W/cm^2 , a standard value in microchannel studies.

The following part aims to evaluate the integrated HCPV-MCHS system, the boundary conditions of which are illustrated in Fig. 6. Since the top surface of the HCPV cell experienced varied direct solar

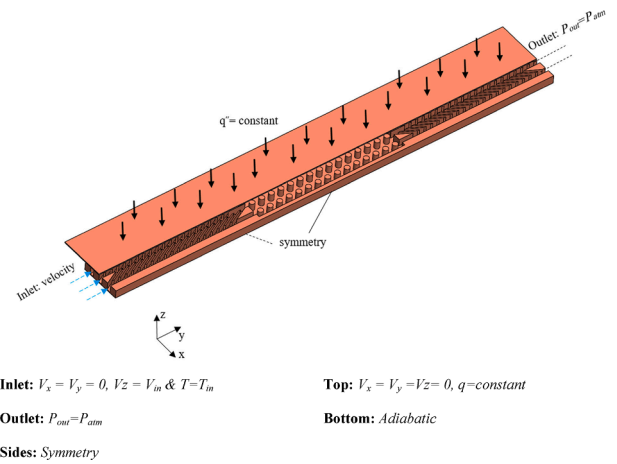


Fig. 5. Boundary conditions for deriving optimal thermal performance of microchannel.

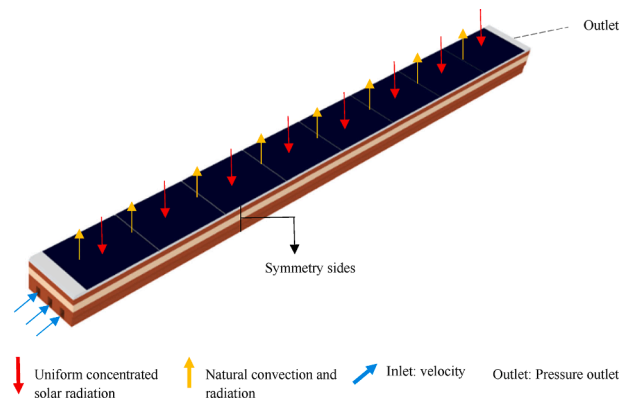


Fig. 6. The boundary conditions and computational domain related to HCPV cell.

irradiance along with convective and radiative heat losses, it was configured with realistic parameters consisting of ambient temperature, wind-driven convective heat transfer coefficient, external radiation temperature, and emissivity. The side walls were assumed to be symmetrical, the inlet coolant temperature and velocity were assumed to be uniform, and the output pressure was assumed to be the same as the atmospheric pressure. Furthermore, at the solid–liquid interface, with the conservation of heat flux being applied, both the solid and liquid phases maintained an equal temperature. Lastly, a non-slip boundary condition was used on the inner walls, meaning the flow velocity remained zero.

3.3. Mesh independence and validation

Ensuring grid independence is essential to not just the accuracy of results, but to computational time and costs as well. To assess mesh independence, four distinct grids, generated by the Meshing Module in ANSYS Fluent V.21, were utilized for domain discretization, constituting nearly 1×10^6 , 2×10^6 , 3×10^6 , and 4×10^6 . According to Fig. 7, as the number of mesh rose, the difference in the Nusselt number between the second and third meshes relative to the fourth (the finest grid) diminished from 2.16 % to 0.39 %. Given the balance between computational accuracy and cost, the grid with 3×10^6 meshes was determined to be the optimal grid. Moreover, the computational results were compared with the experimental data reported in the reference (Sui et al. 2011) to ensure the validity of the simulation results [42]. As depicted in Fig. 8, the average deviation of the average Nusselt number as well as the

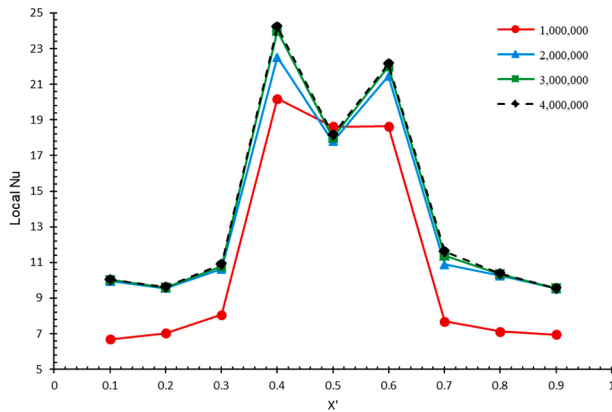


Fig. 7. The investigation of grid independence by local Nusselt number versus the normalized location of microchannel.

friction factor between the computational results and the experimental data was investigated. Regarding the average Nusselt number, the maximum difference between experimental and computational values was 6.14 % at the Reynold number of 300, while the minimum figure was reported at the Reynold number of 700, at 3.82 %, showing that the validity of the results was ensured. Similarly, the comparison of the results for the friction factor indicates that the differences were in a reliable range of agreement, with a maximum difference of 10.82 % and a minimum of 2.28 % at the Reynolds numbers of 600 and 700, respectively.

4. MCHS results and discussion

This section evaluates the performance of 19 hybrid patterns based on flow contours and heat transfer parameters, such as the Nusselt number and pressure drop. This assessment aims to identify optimal thermal performance.

4.1. Flow and temperature characterization

4.1.1. Temperature contours

The analysis commences with an examination of temperature contours. Fig. 9 illustrates the longitudinal temperature contours for patterns with the highest and lowest performances, namely Ellipse I, Circle IV, Rectangle II, and Ellipse II. As can be seen, after the flow entered the MCHS, the fluid temperature increased along the channel. The varied

temperature distributions in the middle parts of the MCHS were attributed to the distinct pin fin patterns. Additionally, Fig. 9 reveals a lower temperature difference among pin fin arrays in Ellipse I compared to the other cases. As such, hotspot generation was prevented due to a more uniform temperature distribution throughout the heat sink. The higher temperature around the pin fins in the lowest row arose from the oblique grooves' orientation in the MCHS inlet. The grooves drove the flow upward, thus increasing the flow velocity, interaction, and cooling capacity of the highest row. In enabling ample flow in both the longitudinal and lateral gaps between adjacent pin fins, Ellipse I's orientation minimized flow blockage and maximized heat transfer. When comparing Ellipse I and Circle IV, differences related to the orientation and wetted surface were observed. Ellipse I possessed a more extended wetted area than Circle IV. While the upper section of Circle IV was unoccupied, allowing fluid to easily cross, the pin fin's side curvature increased flow mixing, leading to enhanced cooling. Being perpendicular to the flow, the pin fins of Ellipse II and Rectangle II maximized flow blockage and created low-velocity recirculation zones. As depicted in Fig. 9, these zones caused fluid entrapment and a temperature increase, ultimately reducing heat transfer in these regions. Among the patterns perpendicular to the flow, Rectangle II enabled higher flow disturbance in light of its sharp edges, thereby having more cooling than Ellipse II. Therefore, it is highlighted that both the wetted area and pattern conforming with the streamlines played major roles in the temperature distribution uniformity and heat transfer rate.

4.1.2. Velocity contours

This section studies the velocity distributions of each pattern and their contributions to heat transfer. Fig. 10 depicts the longitudinal velocity distributions of each pattern at $Re = 1250$. Observably, Ellipse I mixed the flow between the pin fins and channel walls and disturbed the velocity boundary layer. Moreover, as evident in the longitudinal cross-section, the low-volume flow recirculation zones were formed downstream of the pin fins, contributing positively to heat transfer enhancement. Ellipse I had an almost uniform flow distribution, while other patterns failed to achieve such distribution. In Circle IV, for instance, fluid passed through half of the channel without obstruction, which is a drawback for heat transfer. In areas with curvature, however, the interaction between the channel walls and pin fins strengthened flow mixing, enhancing overall heat transfer. For the crossflow patterns, Rectangle II and Ellipse II, a large recirculation area, known as the dead zone, formed downstream of the pin fins (the blue zones). The orientation of pin fins relative to the flow direction narrowed the lateral gap between them, markedly hindering flow and shrinking the cooling rate. As demonstrated in Fig. 10, Ellipse I reported a top velocity of 9.5 m/s,

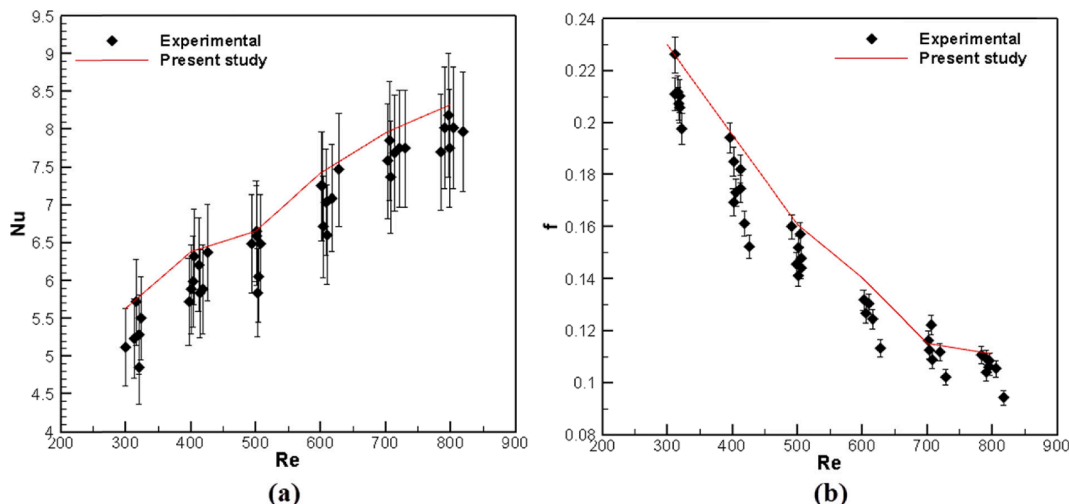


Fig. 8. Comparison of (a) average Nusselt number and (b) friction factor validation with Sui et al. [42].

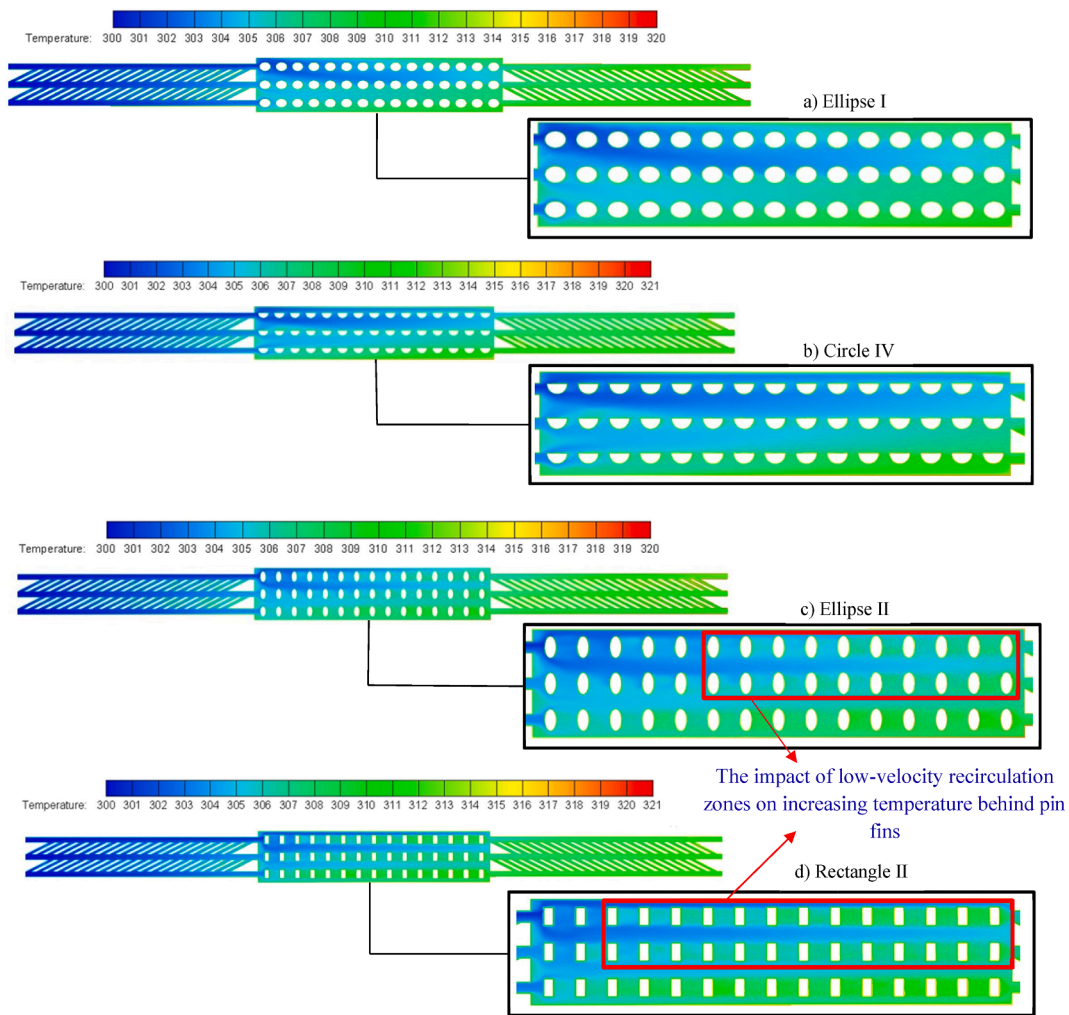


Fig. 9. The temperature distributions for the cases of (a) Ellipse I, (b) Circle IV, (c) Ellipse II, and (d) Rectangle II at $Re = 1250$.

followed closely by Circle IV with a velocity of 9 m/s. Additionally, the lowest row of pin fins exhibited higher temperatures than the uppermost row due to the orientation of the grooves.

Fig. 11 shows the velocity contours at the beginning, middle, and end of the MCHS for different pin fin patterns. By taking a closer look at these contours, a significant correlation can be inferred between the volume of low-velocity recirculation zones formed behind pin fins and the performance parameters of heat sinks. As observed, the configuration of Ellipse I demonstrated flow behavior similar to streamlined geometry, and the regions of low-velocity recirculation behind the pin fins were confined. The decrease of such regions is also significant in the configuration of Circle IV. In contrast, the growth of low-velocity recirculation regions behind the pin fins was noticeable in Ellipse II and Rectangular II. The expansion of these zones had a detrimental effect on heat transfer, causing additional pressure drop without better thermal performance. This phenomenon's impact was significant in that it resulted in the achievement of a maximum Nu in Ellipse I and a maximum pressure drop penalty in Ellipse II.

4.2. Heat transfer and pressure drop

This section analyzes the Nusselt number and pressure drop for each pattern tested. Fig. 12 illustrates the average Nusselt number for various hybrid designs at a Reynolds number of 1250. As shown, an 8 % difference was measured between Ellipse I and II, with the former charting the highest Nusselt number of 65.44, and the latter showing the lowest,

at 60.56. The elliptical pattern had higher heat transfer than other patterns due to its orientation relative to the flow direction. In other words, since it conformed with streamlines, the elliptical design minimized low-velocity recirculation zones, thus contributing to heat transfer improvement.

Furthermore, the heat transfer rates of the triangular patterns were found to be in the order of Triangle II > Triangle IV > Triangle III > Triangle, with the performance difference owed to the distinct behaviors of fluid flow around various triangular pin fins. Among the four-sided designs, the diamond, rectangular, trapezoidal, and square pin fin patterns secured the first through fourth positions, respectively. Additionally, the hexagonal pattern demonstrated higher heat transfer performance among the regular polygons compared to the pentagonal one. Therefore, the patterns in which streamlines were consistent with geometry boundaries showed higher Nusselt numbers.

The pressure drop of each pattern at a Reynolds number of 1250 is depicted in Fig. 13. As can be seen, Ellipse II had the highest pressure drop at 150.2 kPa, while Trapezoid II had the lowest at 113.4 kPa. Ellipse II's more considerable pressure drop can be associated with its orientation being perpendicular to the flow, a placement which reduced lateral space for the fluid flow, thus leading to a large stagnation zone developing between consecutive pin fins. Patterns that conformed with the streamlines typically exhibited a reduced pressure drop compared to others. Moreover, attributing to their configurations, the pressure drops of the triangular pin fins were observed to be in the order of Triangle II > Triangle IV > Triangle I > Triangle III. In other words, the first side of

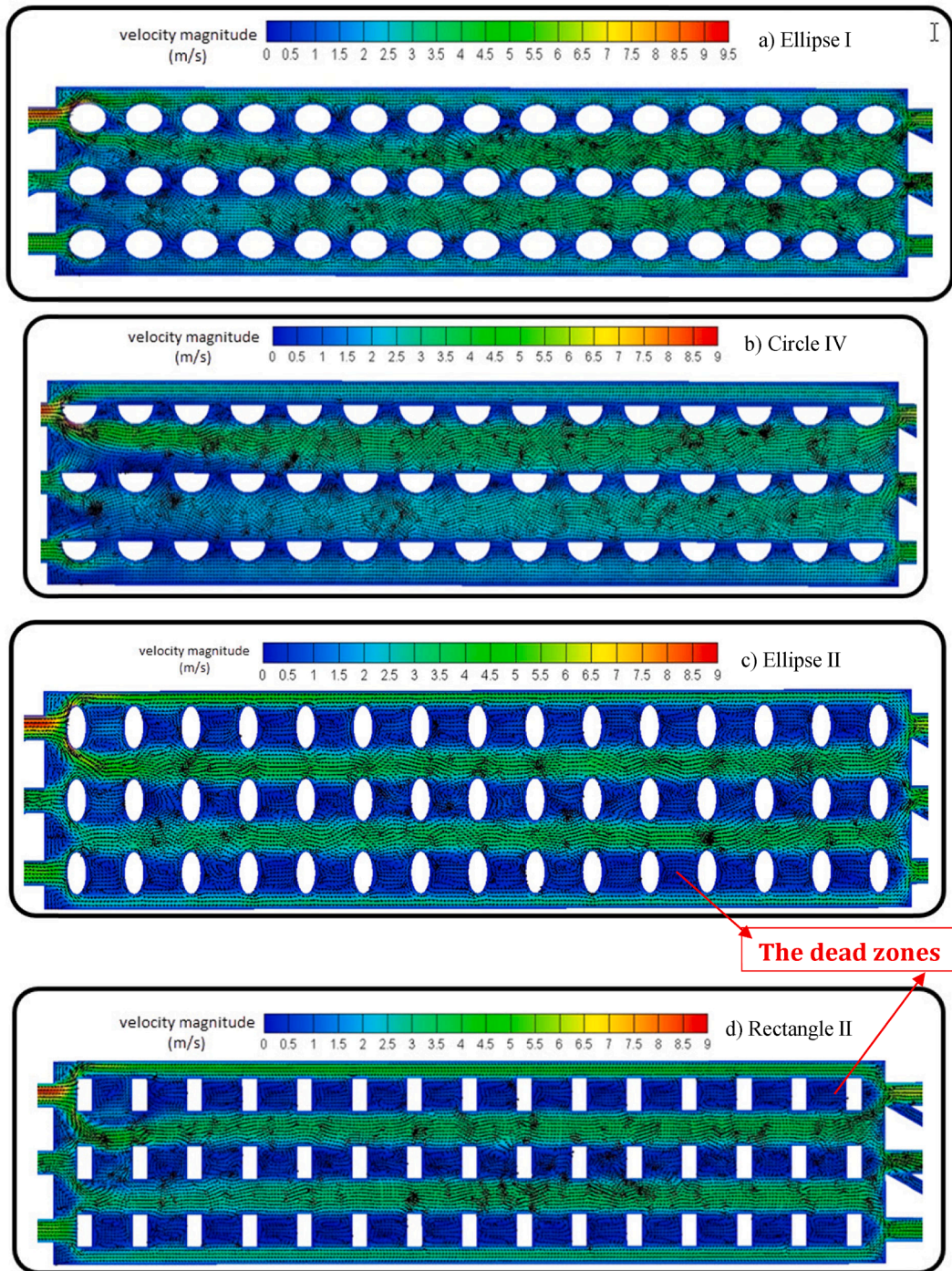


Fig. 10. The velocity distributions for the cases of (a) Ellipse I, (b) Circle IV, (c) Rectangle II, and (d) Ellipse II at $Re = 1250$.

Triangle II, which was perpendicular to the flow, imposed significant blockage effects, leading to the most substantial pressure drop. Triangle IV had a similar structure to Triangle II, except that it was split in the middle, with the top mixing the flow and the bottom imposing no significant obstruction. The orientation of the sides in Triangle III and Triangle I resulted in minimal flow mixing between the wall and fluid, leading to reduced pressure drops. Among the four-sided patterns, the diamond pin fin pattern reported the highest pressure drop (135.4 kPa), while Rectangle II led to the second highest. The orientation of the diamond pattern and Rectangle II can explain the reason behind their larger pressure drops. The trapezoidal pattern resulted in the lowest pressure drop among the four-sided patterns because it conformed with

flow streamlines. Among the regular polygons, the hexagonal pattern had a higher pressure drop than the pentagonal. Additionally, among the circular designs, Circle III exhibited the most significant pressure drop due to its perpendicular side relative to the main flow. Furthermore, there was a difference in pressure drop between the two semi-circles, Circle II and Circle IV, which arose from the impingement flow. In other words, due to the upward orientation of the oblique grooves, the flow velocity was greater at the upper section of the MCHS. As a result, Circle II imposed a more considerable pressure drop on the system than Circle IV due to its side curvature.

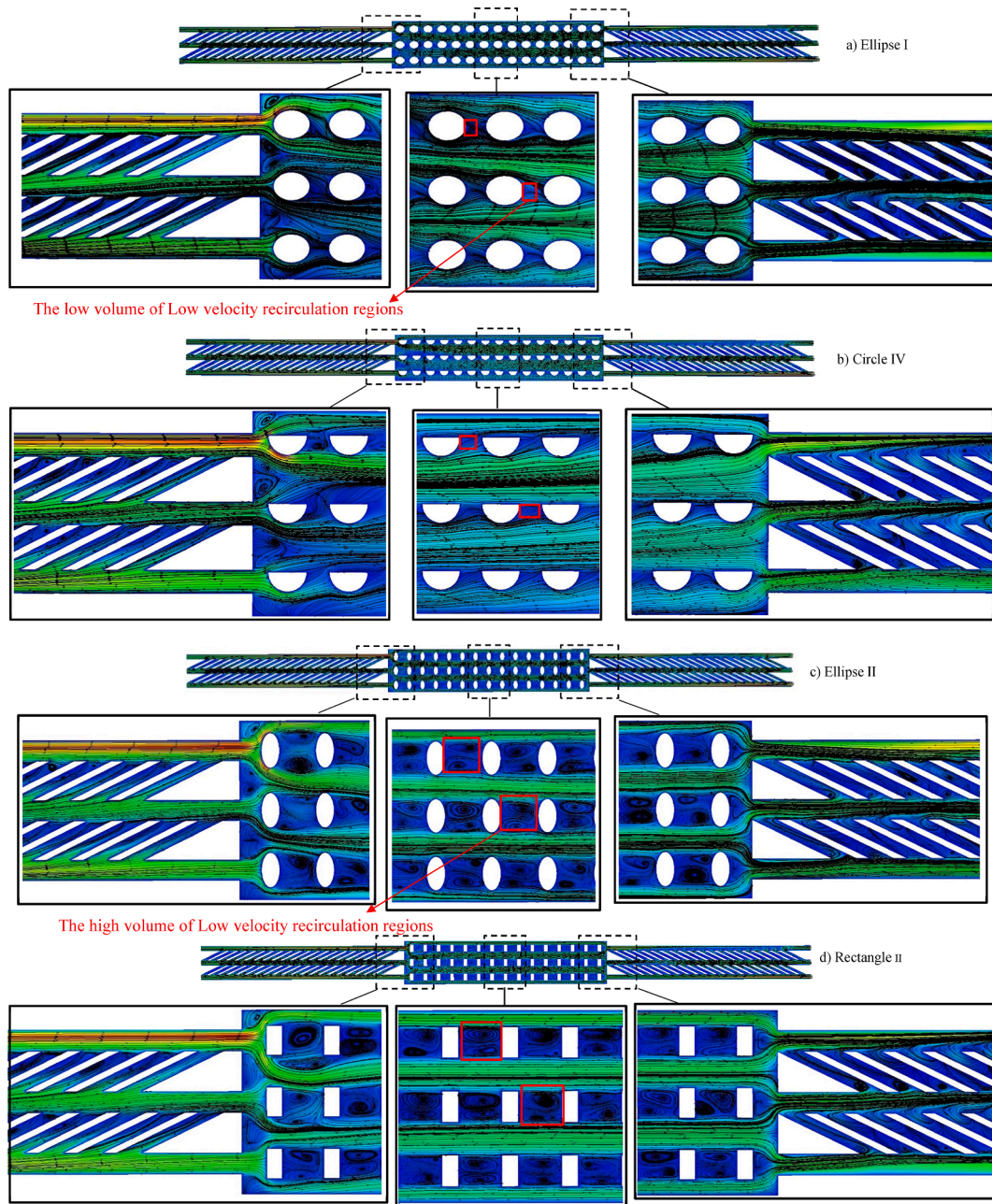


Fig. 11. The velocity contours at the beginning, in the middle, and at the end of the MCHS for cases of (a) Ellipse I, (b) Circle IV, (c) Rectangle II, and (d) Ellipse II at $Re = 1250$.

4.3. Performance evaluation index

To more effectively assess the efficiency of the hybrid MCHS, equation (19) is utilized. This equation compares the rise in the Nusselt number and pressure drop with a reference model [43]. The reference model was taken to be the rectangular pin fin pattern, given its prevalent use in this field.

$$\eta = \frac{Nu_{Pin-fin} / Nu_{Rectangularpin-fin}}{(\Delta P_{Pin-fin} / \Delta P_{Rectangularpin-fin})^{\frac{1}{3}}} = \frac{(ENu)}{(E\Delta P)^{\frac{1}{3}}} \quad (19)$$

Fig. 14 shows the performance coefficients (η) for the studied patterns. A performance coefficient exceeding 1 indicates higher performance compared to the reference model, while a η value below 1 suggests lower relative performance. According to Fig. 14, Ellipse I showed the highest performance coefficient with 1.05, while Ellipse II had the lowest figure

of 0.92. Interestingly, Trapezoid II had the third-best performance with 1.03 despite its low heat transfer capability, attributed to its reduced pressure drop. Observably, patterns that conformed with the streamlines outperformed those shapes with perpendicular sides relative to the main flow. Patterns oriented perpendicular to the flow direction recorded a performance coefficient under one, making them less suitable for cooling systems. The pin fin patterns were evaluated in terms of thermal performance and flow parameters to find the optimal patterns, with the elliptical pin fin showing the highest performance in dissipation heat. In the next phase of our research, we evaluated an HCPV cell's electrical and thermal performances as it was cooled by the hybrid configuration, a combination of oblique grooved microchannels and elliptical pin fins.

5. HCPV cell results and discussion

Elevated PV cell temperatures adversely affect electrical efficiency.

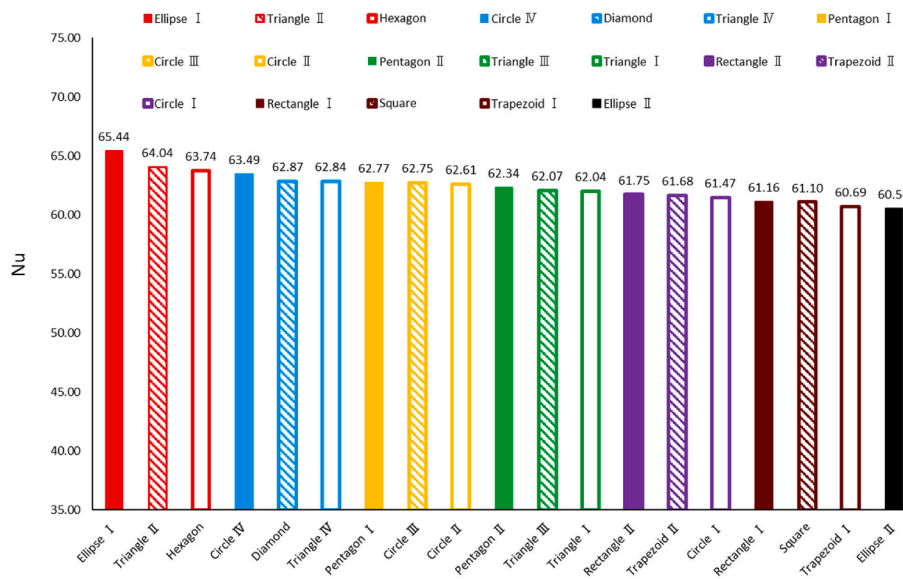


Fig. 12. Average Nusselt number for all geometries at Re = 1250.

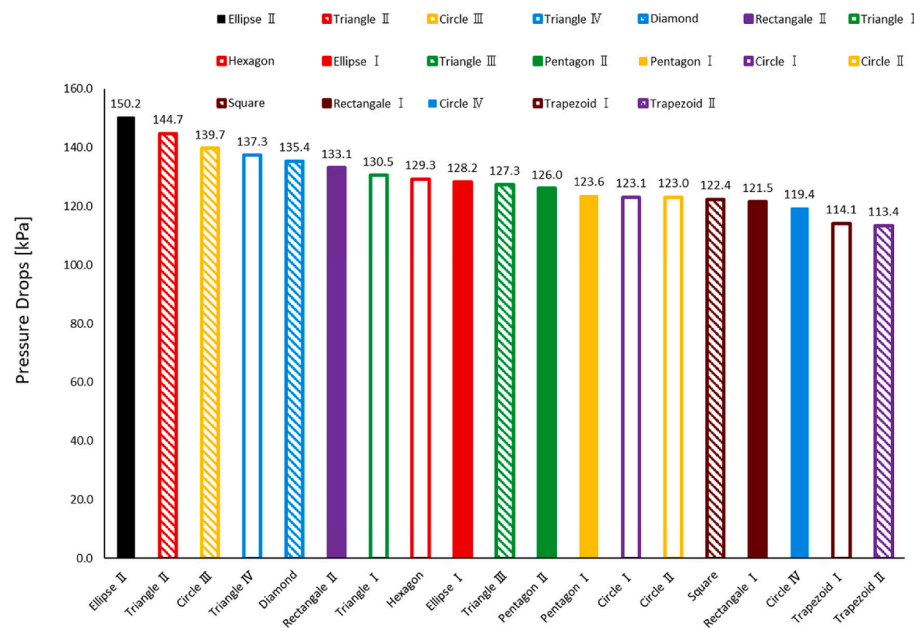


Fig. 13. Pressure drops of all cases at Re = 1250.

For these cells, the recommended optimal operational temperature ranges from 301 to 353 K. Most notably, an increment of 1 K in temperature leads to a 0.5 % decrement in electrical efficiency [5]. As such, maintaining a solar cell temperature close to 301 K becomes essential for achieving peak electrical performance. An efficient cooling mechanism is therefore necessary to effectively dissipate the generated heat and contribute positively to the PV system’s durability.

In this part of our research, we simulated the integrated HCPV-MCHS system maintaining a stable HCPV cell temperature of nearly 301 K. Then, we evaluated the operating parameters, such as pressure drop, PV temperature uniformity, power generation, and pumping power, as well as the required flow rate to remove solar heat flux. The results were compared to straight MCHS, the most commonly used microchannel in commercial applications. Subsection 5.1 discusses the collection of climatic data in the case study region. Subsection 5.2 describes the effects of operating parameters, like coolant flow rate, to hold a constant PV cell

temperature of 301 K throughout different months of the year in both the proposed pattern and straight MCHS. Subsection 5.3 discusses the pressure drop in the straight and hybrid MCHS models. Subsection 5.4 incorporates the power generation and pumping power results. Finally, subsection 5.5 discusses the local temperature distribution on the PV cell as it was cooled by the hybrid pattern.

5.1. Collection of climatic data

Collected data related to outdoor temperatures and wind velocities was sourced from the official portal of the Iran Meteorological Organization [44]. Subsequently, the Solar Ray Tracing feature in ANSYS Fluent was employed to determine the direct solar irradiance on the PV cell. Shiraz, located at 52.5836° N and 52.5836° E, is identified as a city in Iran renowned for its significant irradiance potential. The simulations were performed for the hottest day of each season in 2021, including 31

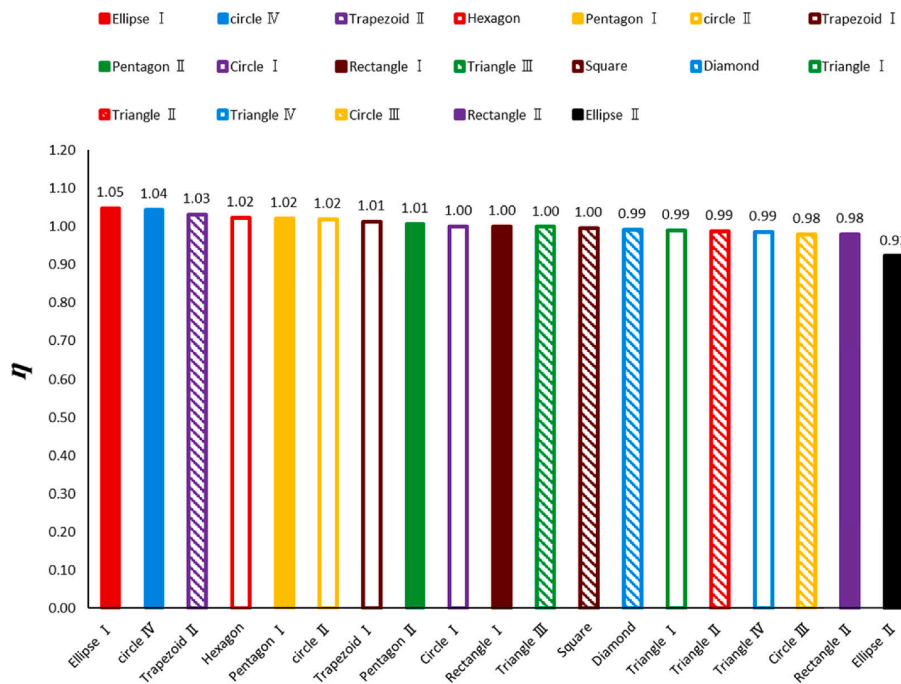


Fig. 14. Performance evaluation criteria index related to all the cases at $Re = 1250$.

May, 1 December, 6 September, and 9 July, spanning from 06:00 to 19:00. Fig. 15 illustrates these findings. As can be seen, the highest irradiance occurred in summer (325 W/m² at 15:00), which raised the temperature of the PV cell to 370 K.

Due to wind speed variations, the solar heat was not symmetrical. This asymmetry represents a novel aspect of this study since many researchers typically operate under the presumption of symmetrical solar radiation. As previously noted, a solar concentration lens was used to concentrate solar radiation on the PV cell’s target area to maximize power generation. To simulate an HCPV system, the solar heat flux was multiplied by $CR = 1000$.

5.2. Effect of the flow rate on HCPV cell performance

Fig. 16 depicts the mass flow rate required to maintain the HCPV temperature at 301 K during the day using the hybrid MCHS. As can be seen, compared to the straight pattern, the hybrid configuration demanded a reduced flow rate for effective heat dissipation. The maximum flow rate in the straight MCHS stood at 264 ml/min in the summer, while the hybrid pattern required only 42 ml/min. The hybrid model’s higher efficiency could be explained by the increased flow mixing, which lead to the periodic disruption of boundary layers. Furthermore, the hybrid model possessed a larger wetted area, which significantly enhanced heat transfer. Observations indicated that, in the spring, the hybrid model sustained a consistent temperature of 301 K with an average flow rate of 30 ml/min throughout the entire day. On the other hand, the straight MCHS failed to keep the average temperature stable at 301 K during 12:00–16:00 (Zone 1). Likewise, in the summer, the straight MCHS also failed to keep the HCPV cell cool for a larger portion of the day (Zone 1). In contrast, the hybrid model effectively maintained a constant temperature of 301 K in this zone with an average flow rate of approximately 90 ml/min.

During peak irradiance periods in fall and winter (Zones 1 and 2), the straight MCHS was inefficient. The hybrid MCHS, however, removed heat with average flow rates not surpassing 45 ml/min. An advantage of this present study is that a much smaller coolant flow rate was required to cool the HCPV cell compared to earlier works. This difference demonstrated the efficient performance of the proposed hybrid

configuration.

5.3. Analysis of pressure drop

The pressure drop is vital when assessing PV power generation and electrical efficiency. Evaluating the pressure drop assists in choosing the most suitable pump for the system. Fig. 17 illustrates the variations in MCHS pressure drop over distinct seasons. As anticipated, there was a direct correlation between the pressure drop and the flow rate. An increase in the flow rate resulted in an increased pressure drop. As can be seen, the straight MCHS required a larger coolant flow rate, which imposed a larger pressure drop on the system. In other words, a low thermal performance necessitated a larger flow rate to improve heat transfer, which resulted in an increased pressure drop. To illustrate this, at 12:00 in the spring, the straight MCHS demanded a flow rate nearly seven times as much as the hybrid configuration. In the summer, the maximum pressure drop in the hybrid pattern was 618 kPa. Fig. 17 shows the zones in which the straight MCHS was inefficient in removing solar heat flux. It should be noted that the straight MCHS imposed a larger pressure drop than the hybrid configuration at a given flow rate.

5.4. Output power and pump power consumption

Pumps are major components in conveying a coolant through the system. Therefore, it is important to calculate pump power. Since higher pumping power is required to handle the pressure drop at higher flow rates, the flow rate should be accurately monitored to secure a trade-off between thermal performance and pump power. Unlike earlier works [29,39] which applied a constant flow rate to cool PV cells, this study calculated different flow rates at different times based on the cooling demand in order to minimize pumping power and maximize output power. As shown in Fig. 18, the straight MCHS had higher pumping power than the hybrid MCHS because it required a larger flow rate, imposing a larger pressure drop. For example, the straight MCHS reported a pumping power of nearly 1290 mW in spring at 11:00, approximately 30 times higher than the hybrid MCHS (40 mW). Furthermore, the straight MCHS was inefficient most of the day due to its poor thermal performance. While the hybrid MCHS required an

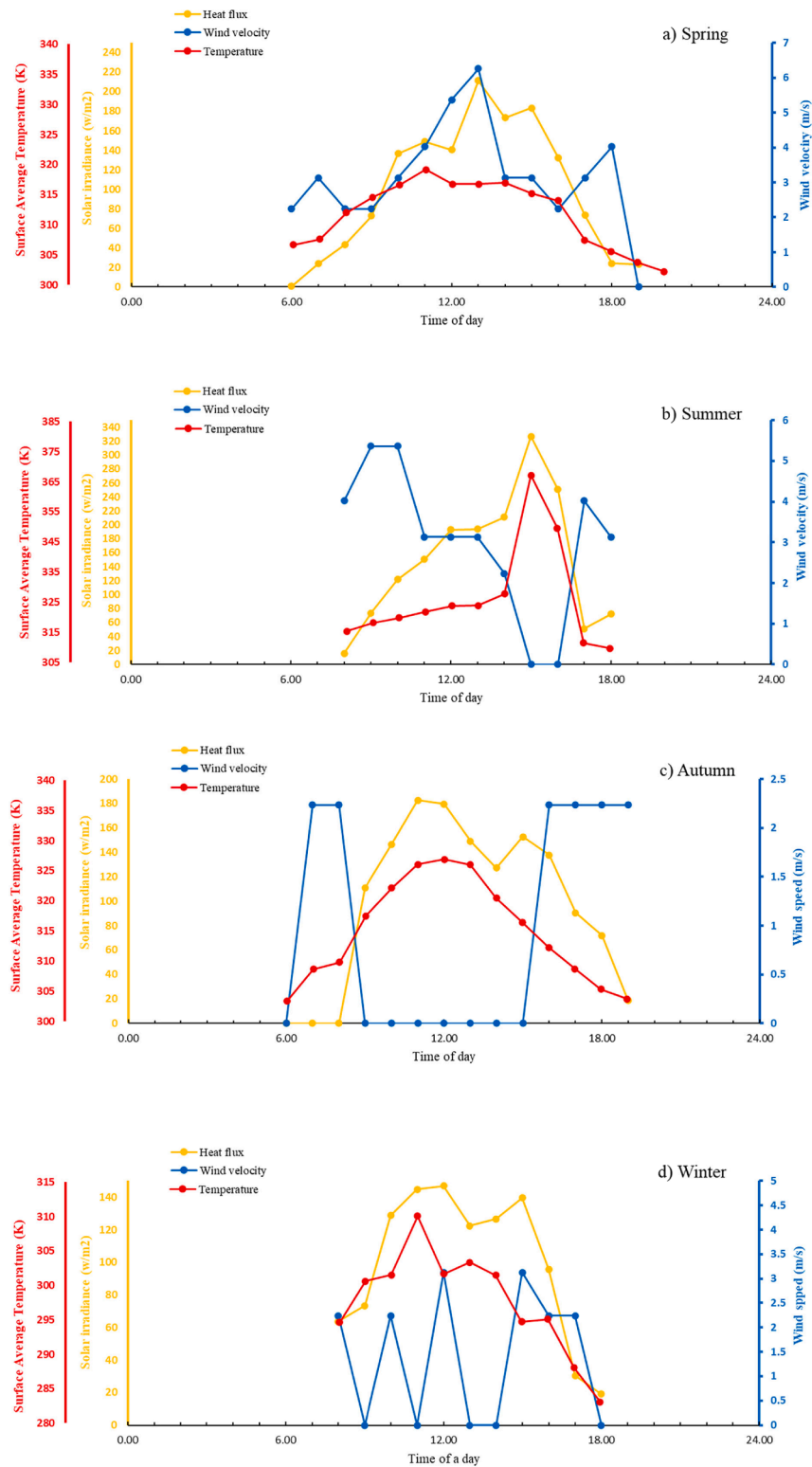


Fig. 15. The evaluated surface average temperature, solar irradiance, and wind velocity for (a) spring, (b) summer, (c) autumn, and (d) winter.

average pumping power of 240 mW over the course of a whole day in the summer, for other seasons, this figure did not exceed about 60 mW.

Fig. 19 shows the output and pumping power of the optimal hybrid MCHS. The output power, calculated using Eq. (3), depends on the solar cell's electrical efficiency, absorption factor, top layer surface area, and net concentrated irradiance. Pumping power was low at most hours; however, at some times with higher irradiance, it increased to hold a

constant temperature of 301 K. For example, the highest and lowest output power in summer was 2.8 and 0.2 W, with the pumping power of 1500 and 10 mW, respectively. As mentioned, the output power is directly related to the surface area. To save computation time and cost, this study evaluated a small geometry domain to obtain the output power. The simulation of the entire domain, however, would increase the output power under a larger cell surface area. As shown in Table 3,

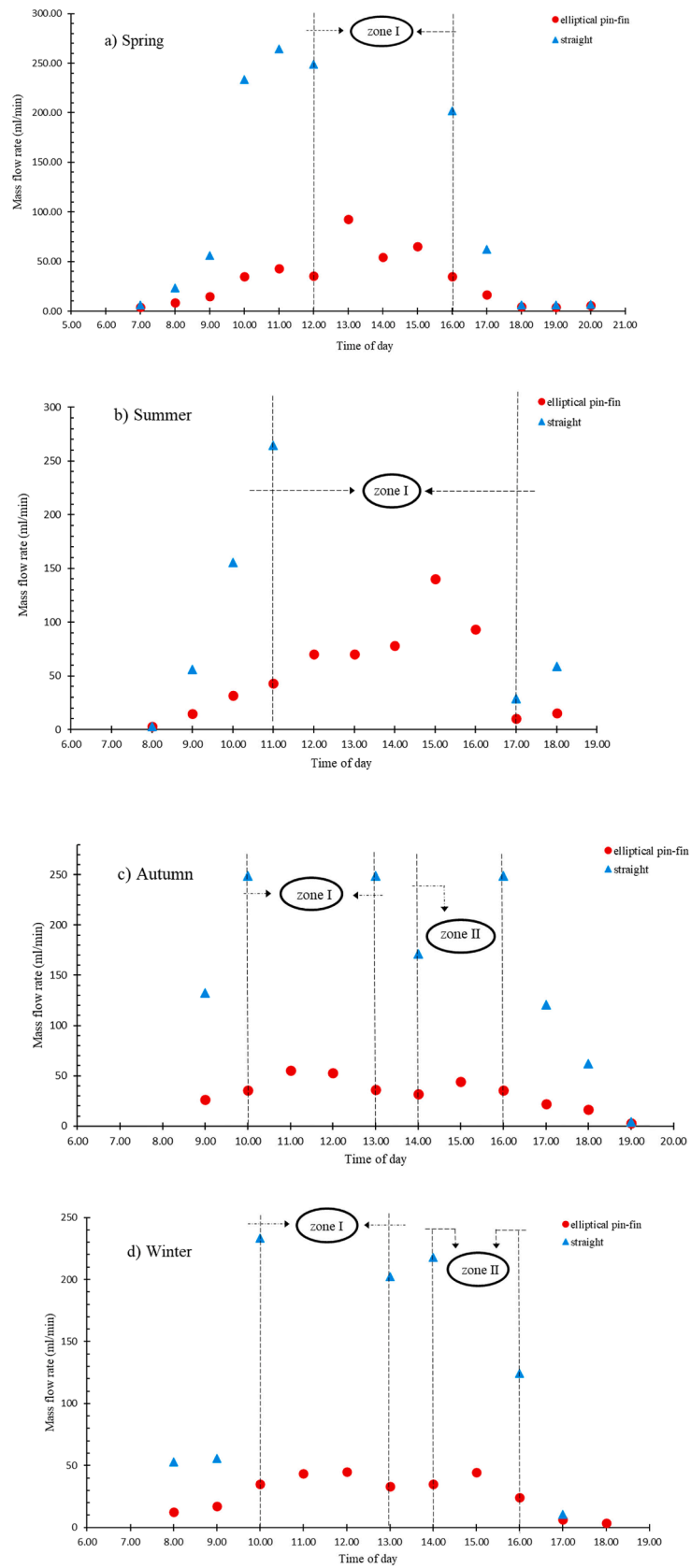


Fig. 16. The comparison of mass flow rate concerning hybrid and straight patterns required to hold the HCPV cell temperature constant at 301 K for (a) spring, (b) summer, (c) autumn, and (d) winter.

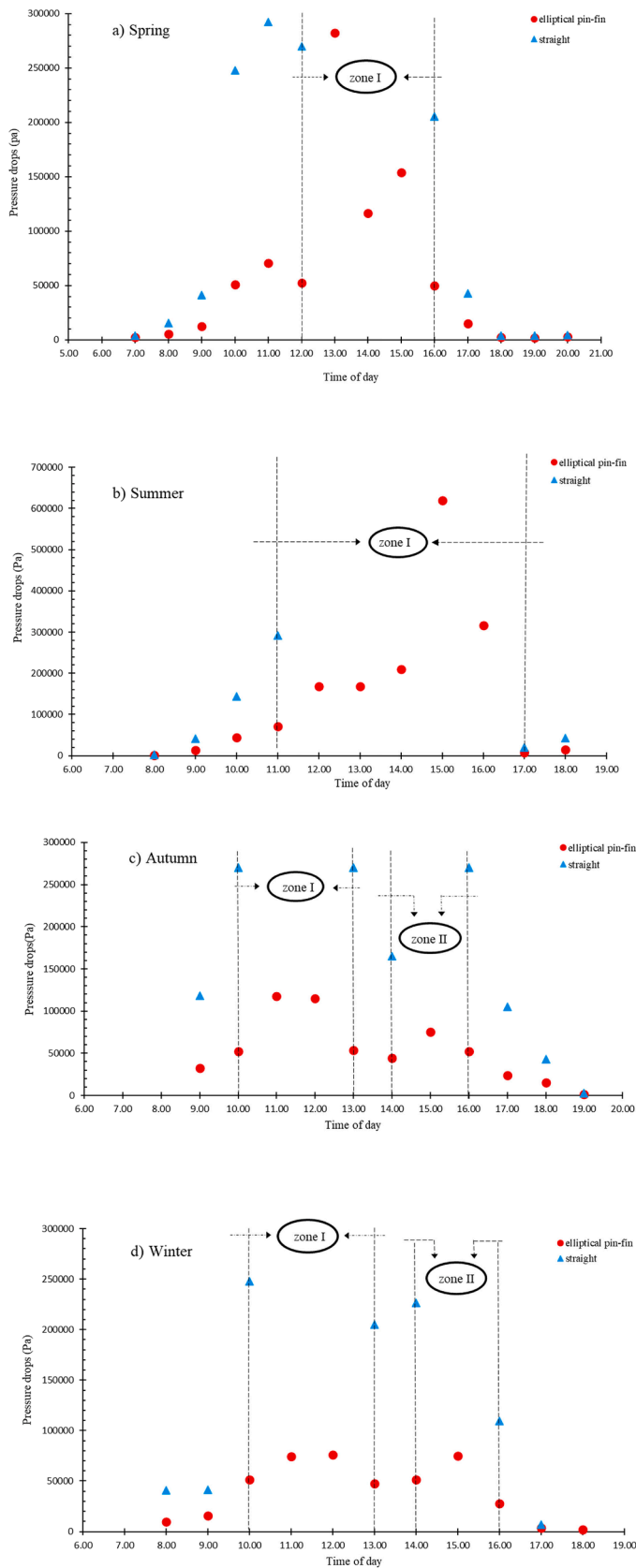


Fig. 17. The comparison of pressure drops imposed on hybrid and straight patterns for (a) spring, (b) summer, (c) autumn, and (d) winter.

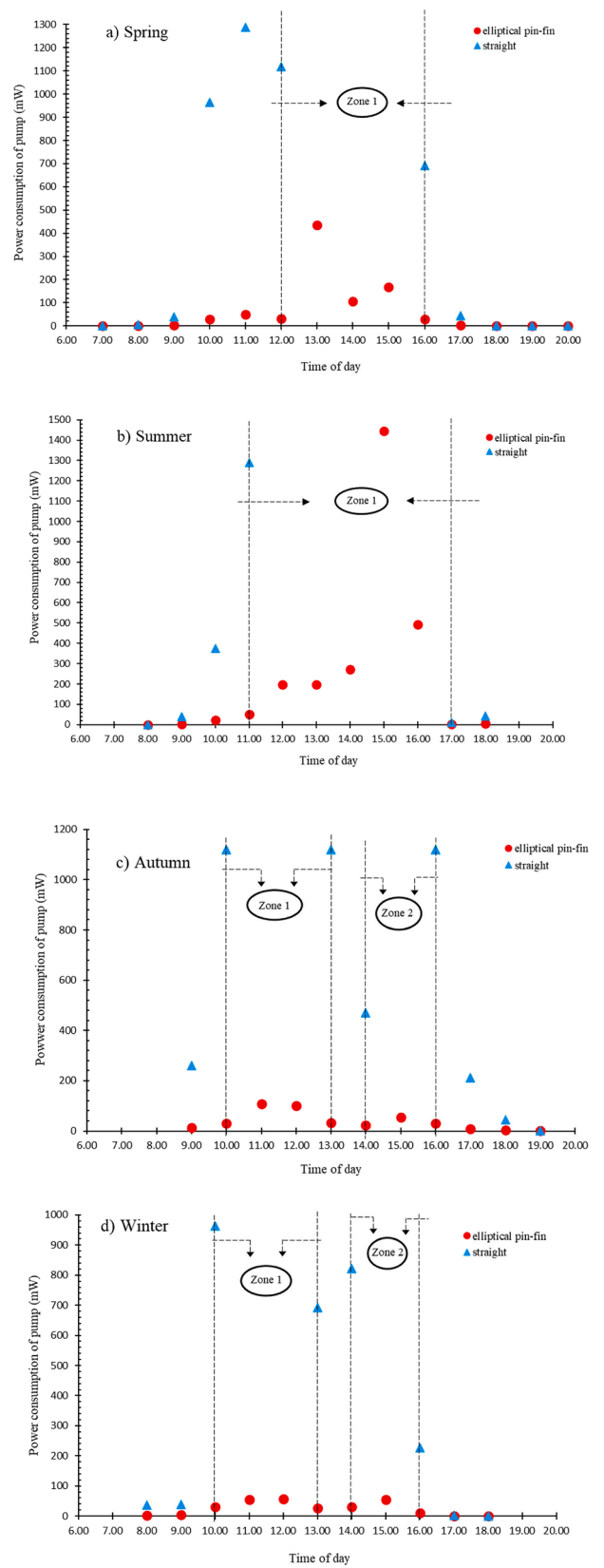


Fig. 18. The comparison of pumping power consumption related to hybrid and straight patterns for (a) spring, (b) summer, (c) autumn, and (d) winter.

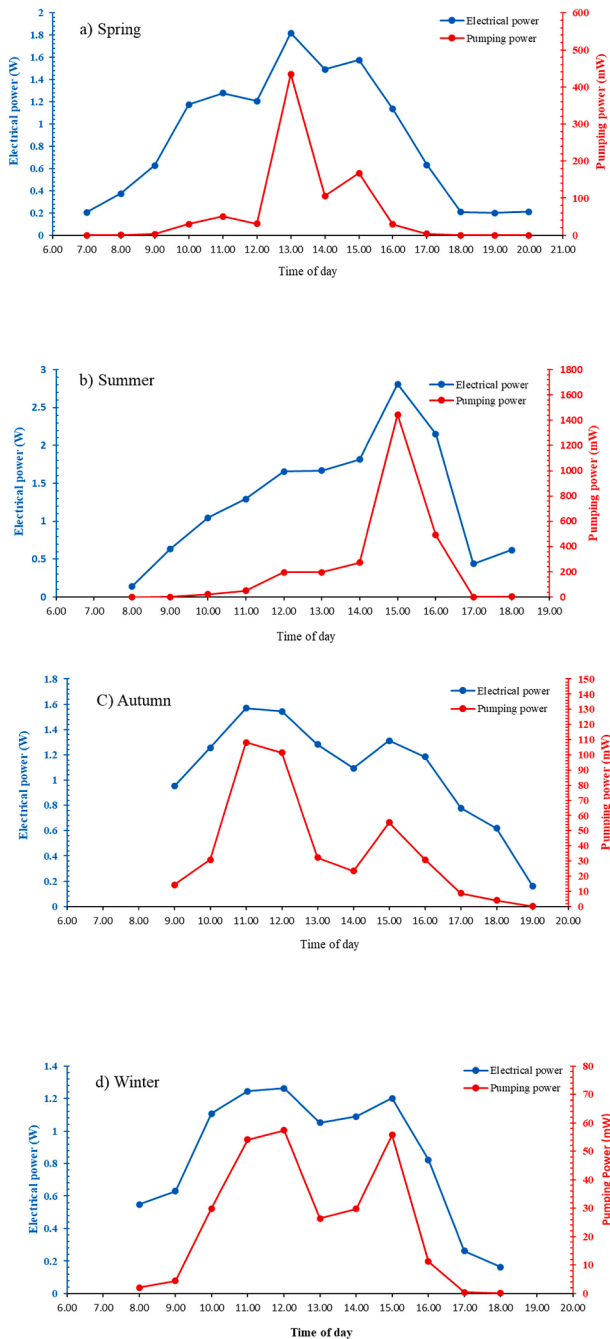


Fig. 19. The comparison of electrical power and pumping power consumption related to hybrid pattern for (a) spring, (b) summer, (c) autumn, and (d) winter.

the maximum output power was 18.443 W, suggesting that the studied HCPV system performed with higher efficiency under actual boundary conditions. In contrast to previous studies, this study reported the exact pumping power. As can be seen in Table 3, 6–8% of the output power was consumed by the pump at peak irradiance hours, whereas up to only 2 % of the output power was consumed at off-peak irradiance hours, with the remaining portion of power exported to the power grid.

5.5. Local temperature distribution and uniformity

As previously highlighted, the temperature of a solar cell should not surpass 110 °C in order to prevent degradation of PV performance. Additionally, as outlined in section 5.1, the temperature of an uncooled solar cell can reach up to 370 K when exposed to direct sunlight.

Table 3

The total electrical power and pumping power consumption related to the optimal hybrid pattern for the autumn season.

Time	Output electrical power (W)	Power consumption of pump (W)
9:00	10.585	0.195
10:00	13.964	0.421
11:00	18.443	1.468
12:00	18.148	1.377
13:00	14.246	0.438
14:00	12.158	0.317
15:00	14.589	0.754
16:00	13.154	0.421
17:00	8.641	0.117
18:00	6.872	0.056
19:00	1.810	0.001

Therefore, it is imperative to ensure that the temperature of the photovoltaic cell is evenly cooled at the desirable temperature. Fig. 20 presents the local temperature distribution cooled by the MCHS system during peak irradiance times over various periods. As can be seen, an average temperature of 301 K with a maximum temperature variation of less than 2 K ($\Delta T = T_{max} - T_{min}$) showed a significantly more uniform temperature. For instance, the maximum temperature variation in the winter was 1.1 K, suggesting a markedly uniform temperature distribution.

6. Conclusion

In this study, the cooling effects of a hybrid pattern on high-concentration photovoltaic cells were explored through numerical simulation. The unique hybrid design, seen as this work's central innovation, features a combination of the oblique microchannel and micro pin fin extracted from a comprehensive investigation of 19 pin fin cross sections. Once derived, the optimal configuration was applied to a high-concentration photovoltaic cell to enhance its cooling. Considering parameters such as coolant flow rate, net power generation, and pumping power, the photovoltaic cell's performance was assessed on the hottest day of each season in the city of Shiraz by comparing the hybrid and straight microchannel heat sink models. The following results were drawn:

- Patterns conforming with streamlines minimized flow blockage and confined low-velocity recirculation zones, leading to higher heat transfer rates than perpendicular patterns. While Ellipse I garnered the most significant Nusselt number of 65.44, Ellipse II reported the lowest figure (60.56).
- The largest and smallest pressure drops were reported in Ellipse II and Trapezoid II with 150.2 kPa and 113.4 kPa, respectively.
- The optimal pattern resulted in the photovoltaic cell achieving an electrical efficiency of 40.16 while also maintaining a cell surface temperature of 301 K, with an average flow rate of approximately 30 and 52 ml/min in the spring and summer, respectively.
- While a straight microchannel failed to keep the cell temperature stable at the hottest hours, 11:00 to 17:00 in the summer, the hybrid configuration succeeded in cooling with an average flow rate of 90 ml/min. The hybrid microchannel's higher performance arose from the larger wetted area and flow mixing, leading to the periodic disruption of boundary layers and an enhancement of heat transfer.
- To keep the solar cell at a given temperature, the straight microchannel required a larger coolant flow rate due to poor heat transfer. As such, pumping power would be higher in a straight microchannel than in a hybrid pattern. For example, while the hybrid design's pump power consumption was found to be 40 mW in the spring at 11:00, this figure was found to be 1300 mW in the straight microchannel.

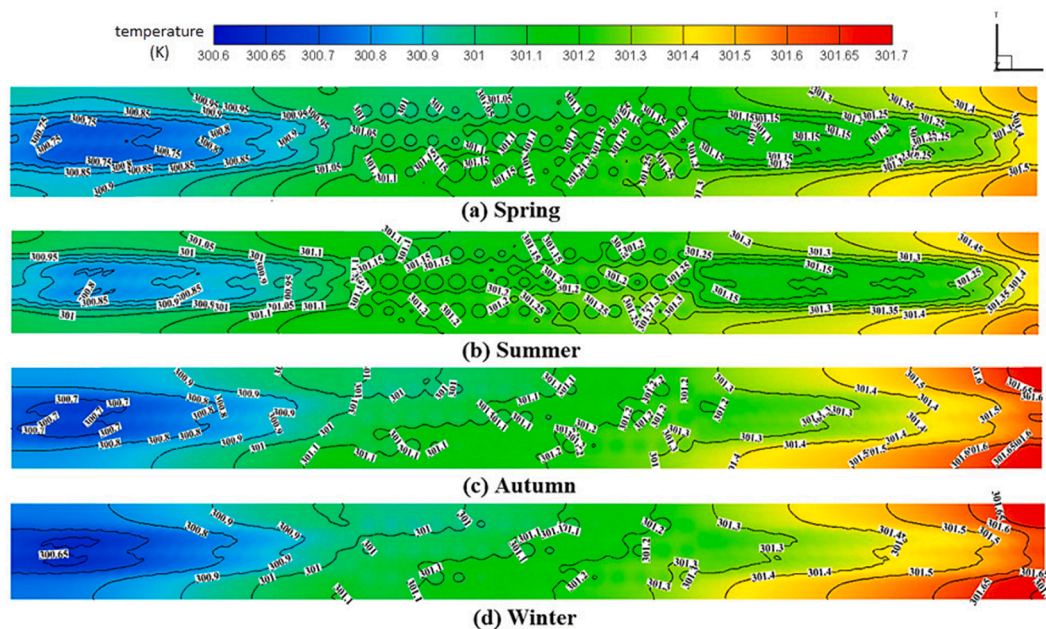


Fig. 20. The temperature distribution on the surface of the HCPV cell at the peak irradiance time for (a) spring, (b) summer, (c) autumn, and (d) winter.

- The maximum output electrical power for the whole domain of the high-concentration photovoltaic cell was 18.443 W in the autumn, with a pumping power contributing to 1.47 W.

7. Future work and direction

Finally, according to the results, some research gaps are recognized, and the following directions are suggested:

- Investigating the optimal placement, spacing, and arrangement of pin fins within the oblique grooved microchannel will assist in achieving even greater thermal performance while further reducing the pressure drop.
- Combining the hybrid design with other advanced cooling techniques can be an exciting topic for the research community. For instance, integrating the hybrid system with techniques such as jet impingement, nanoparticles, or phase change materials could enhance cooling efficiency, especially in high heat flux scenarios.
- Employing advanced flow visualization techniques will be essential in the experimental investigation of hybrid patterns. Researchers can gain a fundamental understanding of fluid dynamics by visualizing the flow behaviors, especially around the pin fins.

CRedit authorship contribution statement

Yousef Alihosseini: Conceptualization, Project administration, Visualization, Writing – review & editing. **Yaser Oghabneshin:** Software, Visualization, Writing – review & editing. **Amir Rezazad Bari:** Formal analysis, Methodology, Writing – original draft. **Sahel Moslemi:** Validation, Visualization, Writing – review & editing. **Ahmad Reza Roozbehi:** Methodology, Software, Validation. **Mohammad Zabetian Targhi:** Supervision, Writing – review & editing. **Wei Guo:** Supervision, Writing – review & editing.

Declaration of competing interest

The authors declare that they have no known competing financial interests or personal relationships that could have appeared to influence the work reported in this paper.

Data availability

Data will be made available on request.

Acknowledgments

Y.A. and W.G. acknowledge the support provided by the National High Magnetic Field Laboratory at Florida State University, which is supported by the National Science Foundation Cooperative Agreement No. DMR-2128556 and the state of Florida.

References

- [1] J. Duan, A novel heat sink for cooling concentrator photovoltaic system using PCM-porous system, *Appl. Therm. Eng.* 186 (2021), 116522.
- [2] M. Ebrahimi, M. Rahimi, A. Rahimi, An experimental study on using natural vaporization for cooling of a photovoltaic solar cell, *Int. Commun. Heat Mass Transfer* 65 (2015) 22–30.
- [3] M. Ahmed, A.M. Radwan, Performance evaluation of new modified low-concentrator polycrystalline silicon photovoltaic/thermal systems, *Energ. Conver. Manage.* 149 (2017) 593–607.
- [4] Z. Wang, D. Kortge, J. Zhu, Z. Zhou, H. Torsina, C. Lee, P. Bermel, Lightweight, passive radiative cooling to enhance concentrating photovoltaics, *Joule* 4 (2020) 2702–2717.
- [5] M. George, A.K. Pandey, N. Abd Rahim, V.V. Tyagi, S. Shahabuddin, R. Saidur, Concentrated photovoltaic thermal systems: A component-by-component view on the developments in the design, heat transfer medium and applications, *Energ. Conver. Manage.* 186 (2019) 15–41.
- [6] N. Gilmore, V. Timchenko, C. Menictas, Microchannel cooling of concentrator photovoltaics: A review, *Renew. Sustain. Energy Rev.* 90 (2018) 1041–1059.
- [7] T. Ma, H. Yang, Y. Zhang, L. Lu, X. Wang, Using phase change materials in photovoltaic systems for thermal regulation and electrical efficiency improvement: a review and outlook, *Renew. Sustain. Energy Rev.* 43 (2015) 1273–1284.
- [8] W. Pang, H. Yu, Y. Zhang, H. Yan, Solar photovoltaic based air cooling system for vehicles, *Renew. Energy* 130 (2019) 25–31.
- [9] N. Arcuri, F. Reda, M. De Simone, Energy and thermo-fluid-dynamics evaluations of photovoltaic panels cooled by water and air, *Sol. Energy* 105 (2014) 147–156.
- [10] S. Ahmed, S. Li, Z. Li, G. Xiao, T. Ma, Enhanced radiative cooling of solar cells by integration with heat pipe, *Appl. Energy* 308 (2022), 118363.
- [11] M. Modjinou, J. Ji, J. Li, W. Yuan, F. Zhou, A numerical and experimental study of micro-channel heat pipe solar photovoltaics thermal system, *Appl. Energy* 206 (2017) 708–722.
- [12] L. Chen, D. Deng, Q. Ma, Y. Yao, X. Xu, Performance evaluation of high concentration photovoltaic cells cooled by microchannels heat sink with serpentine reentrant microchannels, *Appl. Energy* 309 (2022), 118478.
- [13] H.I. Elqady, A. Radwan, A.Y.M. Ali, M. Rabie, E.M. Abo-Zahhad, S. Ookawara, M. F. Elkady, A.H. El-Shazly, Concentrator photovoltaic thermal management using a

- new design of double-layer microchannel heat sink, *Sol. Energy* 220 (2021) 552–570.
- [14] N. Karami, M. Rahimi, Heat transfer enhancement in a hybrid microchannel-photovoltaic cell using Boehmite nanofluid, *Int. Commun. Heat Mass Transfer* 55 (2014) 45–52.
- [15] M. Javidan, A.J. Moghadam, Effective cooling of a photovoltaic module using jet-impingement array and nanofluid coolant, *Int. Commun. Heat Mass Transfer* 137 (2022), 106310.
- [16] Y. Alihosseini, M.Z. Targhi, M.M. Heyhat, N. Ghorbani, Effect of a micro heat sink geometric design on thermo-hydraulic performance: A review, *Appl. Therm. Eng.* 170 (2020), 114974.
- [17] H.G. Teo, P.S. Lee, M.N.A. Hawlader, An active cooling system for photovoltaic modules, *Appl. Energy* 90 (2012) 309–315.
- [18] A.Y.M. Ali, E.M. Abo-Zahhad, M.F. Elkady, S. Ookawara, A.H. El-Shazly, A. Radwan, Temperature uniformity enhancement of densely packed high concentrator photovoltaic module using four quadrants microchannel heat sink, *Sol. Energy* 202 (2020) 446–464.
- [19] Z. Khattak, H.M. Ali, Air cooled heat sink geometries subjected to forced flow: A critical review, *Int. J. Heat Mass Transf.* 130 (2019) 141–161.
- [20] N. Ghorbani, M.Z. Targhi, M.M. Heyhat, Y. Alihosseini, Investigation of wavy microchannel ability on electronic devices cooling with the case study of choosing the most efficient microchannel pattern, *Sci. Rep.* 12 (2022) 5882.
- [21] I.A. Ghani, N.A.C. Sidik, N. Kamaruzaman, Hydrothermal performance of microchannel heat sink: The effect of channel design, *Int. J. Heat Mass Transf.* 107 (2017) 21–44.
- [22] H. Sadique, Q. Murtaza, Samsher, Heat transfer augmentation in microchannel heat sink using secondary flows: A review, *Int. J. Heat Mass Transf.* 194 (2022), 123063.
- [23] H.E. Ahmed, B.H. Salman, A.S. Kherbeet, M.I. Ahmed, Optimization of thermal design of heat sinks: A review, *Int. J. Heat Mass Transf.* 118 (2018) 129–153.
- [24] N. Raja Kuppasamy, R. Saidur, N.N.N. Ghazali, H.A. Mohammed, Numerical study of thermal enhancement in micro channel heat sink with secondary flow, *Int. J. Heat Mass Transf.* 78 (2014) 216–223.
- [25] Y.J. Lee, P.K. Singh, P.S. Lee, Fluid flow and heat transfer investigations on enhanced microchannel heat sink using oblique fins with parametric study, *Int. J. Heat Mass Transf.* 81 (2015) 325–336.
- [26] Y. Alihosseini, M. Zabetian Targhi, M. Mahdi Heyhat, Thermo-hydraulic performance of wavy microchannel heat sink with oblique grooved finned, *Appl. Therm. Eng.* 189 (2021), 116719.
- [27] D. Yang, Y. Wang, G. Ding, Z. Jin, J. Zhao, G. Wang, Numerical and experimental analysis of cooling performance of single-phase array microchannel heat sinks with different pin fin configurations, *Appl. Therm. Eng.* 112 (2017) 1547–1556.
- [28] Z. Zhao, B. Hu, J. He, M. Lin, H. Ke, Effect of fin shapes on flow boiling heat transfer with staggered fin arrays in a heat sink, *Appl. Therm. Eng.* 225 (2023), 120179.
- [29] E.M. Abo-Zahhad, S. Ookawara, A. Radwan, A.H. El-Shazly, M.F. Elkady, Thermal and structure analyses of high concentrator solar cell under confined jet impingement cooling, *Energ. Convers. Manage.* 176 (2018) 39–54.
- [30] A.Y. Ali, E.M. Abo-Zahhad, H.I. Elqady, M. Rabie, M. Elkady, S. Ookawara, A. El-Shazly, A. Radwan, Thermal analysis of high concentrator photovoltaic module using convergent-divergent microchannel heat sink design, *Appl. Therm. Eng.* 183 (2021), 116201.
- [31] A. Radwan, M. Ahmed, The influence of microchannel heat sink configurations on the performance of low concentrator photovoltaic systems, *Appl. Energy* 206 (2017) 594–611.
- [32] 3C44A – with 10x10mm2Concentrator Triple Junction Solar cell., in, 2022.
- [33] J. Zhou, Q. Yi, Y. Wang, Z. Ye, Temperature distribution of photovoltaic module based on finite element simulation, *Sol. Energy* 111 (2015) 97–103.
- [34] S. Singh, S. Agrawal, D.V. Avasthi, Design, modeling and performance analysis of dual channel semitransparent photovoltaic thermal hybrid module in the cold environment, *Energ. Convers. Manage.* 114 (2016) 241–250.
- [35] T.-L. Chou, Z.-H. Shih, H.-F. Hong, C.-N. Han, K.N. Chiang, Thermal Performance Assessment and Validation of High-Concentration Photovoltaic Solar Cell Module, *IEEE Trans. Compon. Packag. Manuf. Technol.* 2 (2012) 578–586.
- [36] J.S. Jayakumar, S.M. Mahajani, J.C. Mandal, P.K. Vijayan, R. Bhoi, Experimental and CFD estimation of heat transfer in helically coiled heat exchangers, *Chem. Eng. Res. Des.* 86 (2008) 221–232.
- [37] O. Hasan, A.F.M. Arif, M.U. Siddiqui, Finite Element Modeling, Analysis, and Life Prediction of Photovoltaic Modules, *J. Sol. Energy Eng.* 136 (2013).
- [38] D.L. Evans, Simplified method for predicting photovoltaic array output, *Sol. Energy* 27 (1981) 555–560.
- [39] E.M. Abo-Zahhad, S. Ookawara, A. Radwan, A.H. El-Shazly, M.F. Elkady, Numerical analyses of hybrid jet impingement/microchannel cooling device for thermal management of high concentrator triple-junction solar cell, *Appl. Energy* 253 (2019), 113538.
- [40] Y. Alihosseini, A.R. Bari, M. Mohammadi, Effective parameters on increasing efficiency of microscale heat sinks and application of liquid cooling in real life, *Advances in Microfluidics and Nanofluids* (2021) 155–178.
- [41] A. Rezazad Bari, M. Zabetian Targhi, M.M. Heyhat, A numerical study on thermo-hydraulic performance of micro pin fin heat sink using hybrid pin fins arrangement for electronic cooling devices, *Int. J. Numer. Meth. Heat Fluid Flow* 33 (2023) 2478–2508.
- [42] Y. Sui, P.S. Lee, C.J. Teo, An experimental study of flow friction and heat transfer in wavy microchannels with rectangular cross section, *Int. J. Therm. Sci.* 50 (2011) 2473–2482.
- [43] R.L. Webb, Performance evaluation criteria for use of enhanced heat transfer surfaces in heat exchanger design, *Int. J. Heat Mass Transf.* 24 (1981) 715–726.
- [44] Iranian Institute for Climate Studies, in, 2022.